Quantitative imaging of chromatin decompaction in living cells

Author(s):
Dultz, Elisa; Mancini, Roberta; Polles, Guido; Vallotton, Pascal; Alber, Frank; Weis, Karsten

Publication date:
2018-07-15

Permanent link:
https://doi.org/10.3929/ethz-b-000279739

Originally published in:
Molecular Biology of the Cell 29(14), https://doi.org/10.1091/mbc.E17-11-0648

Funding acknowledgement:
159731 - Structure and Function of the Nuclear Pore Complex (SNF)

Quantitative imaging of chromatin decompaction in living cells

Elisa Dultz[a,*], Roberta Mancini[a], Guido Polles[b], Pascal Vallotton[a], Frank Alber[b], and Karsten Weis[a]
[a]Institute of Biochemistry, Department of Biology, ETH Zurich, 8093 Zurich, Switzerland; [b]Molecular and Computational Biology, University of Southern California, Los Angeles, CA 90089

ABSTRACT **Chromatin organization is highly dynamic and regulates transcription. Upon transcriptional activation, chromatin is remodeled and referred to as "open," but quantitative and dynamic data of this decompaction process are lacking. Here, we have developed a quantitative high resolution–microscopy assay in living yeast cells to visualize and quantify chromatin dynamics using the *GAL7-10-1* locus as a model system. Upon transcriptional activation of these three clustered genes, we detect an increase of the mean distance across this locus by >100 nm. This decompaction is linked to active transcription but is not sensitive to the histone deacetylase inhibitor trichostatin A or to deletion of the histone acetyl transferase Gcn5. In contrast, the deletion of *SNF2* (encoding the ATPase of the SWI/SNF chromatin remodeling complex) or the deactivation of the histone chaperone complex FACT lead to a strongly reduced decompaction without significant effects on transcriptional induction in FACT mutants. Our findings are consistent with nucleosome remodeling and eviction activities being major contributors to chromatin reorganization during transcription but also suggest that transcription can occur in the absence of detectable decompaction.**

Monitoring Editor
Orna Cohen-Fix
National Institutes of Health

Received: Nov 20, 2017
Revised: Apr 23, 2018
Accepted: May 8, 2018

INTRODUCTION

DNA in the cell nucleus is present as chromatin in a tight complex with histones and other proteins. This complex is central to the spatial organization of the DNA strand by balancing the negative charges of the phosphate backbone and is also crucial for gene regulation. The three-dimensional (3D) chromatin conformation is highly dynamic and remodeled continuously as cells change their physiological states or their transcriptional programs. This remodeling is orchestrated by histone modifiers and chromatin remodelers, which change the interaction between nucleosomes as well as the interaction between histones, DNA, and the protein complement present at a chromatin site, thereby affecting the spatial packing of nucleosomes or their location, mobility, or density.

Activation of transcription typically leads to a change in chromatin conformation manifested in higher accessibility of the DNA to digestion or transposon integration (Tsompana and Buck, 2014). Although the changes in histone occupancy and accessibility have been studied extensively, the quantitative structural changes of chromatin on a single-cell level remain poorly understood, and it is still largely unclear how the activities of chromatin remodeling complexes are spatially and temporally integrated in living cells. The chromatin "opening" associated with transcriptional activation consists of two distinct changes in chromatin structure: spatial decompaction by changes in nucleosome–nucleosome interactions, and linear decompaction by changes in nucleosome density (Even-Faitelson *et al.*, 2016). Both of these processes are thought to be tightly linked to the posttranslational modification of histones, which characterizes transcriptionally active and transcriptionally silent chromatin (Li *et al.*, 2007). In vitro, specific histone modifications directly influence the spatial organization of chromatin by mediating or restricting nucleosome–nucleosome interactions. For example, the acetylation of histone H4 at lysine 16 prevents the interaction between the acetylated tail and a neighboring nucleosome, lowering the propensity to form a compact 30-nm fiber

This article was published online ahead of print in MBoC in Press (http://www.molbiolcell.org/cgi/doi/10.1091/mbc.E17-11-0648) on May 17, 2018.

Author contributions: E.D. and K.W. conceived and designed the work; E.D. and R.M. collected the data; E.D. and R.M. analyzed and interpreted the data; E.D. and P.V. developed code for image analysis; G.P. and F.A. provided modeling; E.D. drafted the article; E.D., R.M., P.V., G.P., F.A., and K.W. critically revised the article.

*Address correspondence to: Elisa Dultz (elisa.dultz@bc.biol.ethz.ch).

Abbreviations used: GST, glutathione *S* transferase; ORF, open reading frame; Pol II, RNA polymerase II; qPCR, quantitative PCR; smFISH, single molecule fluorescence in situ hybridization; TSA, trichostatin A.

(Shogren-Knaak *et al*., 2006). However, no effect on linear chromatin compaction was observed on autosomes in mammalian cells and *C. elegans* upon loss of H4K16 modification during differentiation (Taylor *et al*., 2013; Lau *et al*., 2017). In addition, evidence is accumulating that extended regular higher-order chromatin structures such as a 30-nm fiber do not form in vivo, and that chromatin fibers are present mostly in dispersed states in living cells (Fussner *et al*., 2012; Hsieh *et al*., 2015; Chen *et al*., 2016). This is corroborated by recent visualizations of chromatin chains in intact mammalian nuclei showing that the local appearance of the chromatin fiber is similar in regions of eu- and heterochromatin (Ou *et al*., 2017). It is therefore unclear how local chromatin folding is influenced by histone modifications in vivo.

In addition to their potential to mediate inter- and intrachromosomal interactions and thus to shape the longer-range organization of the chromatin fiber, nucleosomes constitute direct obstacles to the progression of RNA polymerase II (Pol II) during transcription. Histones and entire nucleosomes are therefore evicted from the DNA during transcription by the concerted action of chromatin remodelers such as the SWI/SNF and SWR1 complexes and histone chaperones such as Asf1 and FACT (reviewed in Venkatesh and Workman, 2015). This nucleosome eviction (leading to a lower nucleosome density) would be expected to cause an increase in the effective length of the chromatin fiber, but this has not been investigated in vivo.

To study chromatin dynamics and organization in vivo, we took advantage of the budding yeast *GAL* locus, a highly regulated gene cluster that has served as a paradigm for inducible gene expression. The *GAL* locus comprises the *GAL7*, *GAL10*, and *GAL1* genes located next to each other on chromosome II. These three genes, encoding enzymes required for the metabolism of galactose, are highly regulated, depending on the carbon sources present in the growth medium. The genes are repressed in the presence of glucose, active in the presence of galactose (but the absence of glucose) and "derepressed" in the absence of both glucose and galactose (e.g., in raffinose-containing medium). Intricate regulation of carbon metabolic genes allows *Saccharomyces cerevisiae* to adapt to and successfully compete with other organisms for various sugars present in the environment (New *et al*., 2014).

GAL gene activation involves the recruitment of several histone-modifying enzymes (Carrozza *et al*., 2002; Wang *et al*., 2002; Govind *et al*., 2007) and dramatic reduction of nucleosome occupancy at the locus (Schwabish and Struhl, 2004; Govind *et al*., 2007; Bryant *et al*., 2008). How this affects the chromatin conformation in vivo and to what extent chromatin decompaction and transcriptional activation are interdependent remains unclear. To address these important questions, we developed an assay to visualize chromatin compaction in living cells. Monitoring the distance between two chromosomal loci on either side of the *GAL* locus revealed drastic linear decompaction upon activation of the *GAL* gene cluster. This decompaction was tightly coupled to transcriptional activity. Furthermore, the observed opening was not regulated by histone acetylation but depended on the activity of nucleosome-evicting chromatin remodelers.

RESULTS

An assay to quantitatively analyze transcription-induced chromatin decompaction in living cells

To probe chromatin decompaction during transcription in a quantitative manner in living cells, we developed a microscopy-based assay to follow chromatin conformation in *S. cerevisiae* over time. We chose the *GAL7-GAL10-GAL1* gene cluster as a model system, since it is very well studied and the presence of three coregulated genes spanning ~5.8 kb is expected to give a clear decompaction response. LacO and TetO repeats were introduced on either side of the *GAL* gene cluster or in a control region and visualized with LacI-GFP and TetR-mCherry (Figure 1A). Bright green and red dots were readily detected in all cells (Figure 1A), and their positions were determined using fitting of a Gaussian profile to obtain subpixel resolution of <20 nm in *x* and y and ~35 nm in *z* (Supplemental Figure 1A). Although imaging of live cells introduces potential motion errors, these did not contribute significantly to our measurements (Supplemental Figure 1, B and C). The distance between LacI-GFP- and TetR-mCherry-tagged loci could thus be determined with high precision and was analyzed in cells grown in raffinose (GAL locus derepressed) or stimulated by the addition of glucose (repressed) or galactose (active). In a control region adjacent to but not spanning the *GAL* locus (18 kb between LacO- and TetO-repeat insertion sites), no change in the distribution of measured distances was observed between the different carbon sources (Figure 1B). In contrast, in strains with a distance of 14 or 31 kb between the insertion points of the repeats across the *GAL* locus, the distribution clearly shifted toward larger distances in activated cultures (Figure 1, B and C) increasing from a mean distance of 280 ± 9 nm in raffinose to 410 ± 15 nm in galactose in the 14-kb reporter strain ($n = 7$) and from 370 ± 4 nm to 488 ± 8 nm in the 31-kb reporter strain ($n = 10$; 3D distances; values are means of biological replicates with standard error of the mean). As expected, the deletion of the transcriptional activator Gal4 prevented the induction of the *GAL* gene transcription and also abolished the decompaction response, whereas deletion of the transcriptional repressor Gal80 led to transcription and decompaction already in raffinose-grown cells (Supplemental Figure 2, A and B). Thus, we have developed a microscopy assay that can readily detect chromatin decompaction upon transcriptional activation in living cells.

Next, we analyzed the dynamics of decompaction in time-lapse experiments. For time-lapse experiments, we acquired only single-plane images and analyzed two-dimensional (2D) distances. This simplified assay allowed us to process all control strains and conditions in a single experiment, yet still provided sufficient sensitivity to detect changes in distance as observed in 3D (Figure 1, D–F). Acute induction of the *GAL* genes by addition of galactose to cells growing in raffinose led to an increase in the population mean distance over the course of 20 min (Figure 1D) mimicking the kinetics of transcriptional activation as seen, for example, by quantitative PCR (qPCR) analysis (Green *et al*., 2012). Similarly, the addition of glucose to cells growing in galactose resulted in fast compaction (Figure 1E) corresponding to the rapid shutdown of transcription due to glucose-induced repression. Decompaction could also be induced with faster kinetics within less than 5 min if cells were pregrown in galactose and then repressed with glucose for only 1 h before reinduction with galactose (Figure 1F). In this case, the presence of elevated levels of Gal1 and Gal3 proteins induces a "transcriptional memory" and leads to faster activation (Kundu and Peterson, 2010). Thus, the kinetics of chromatin de- and recompaction closely follows transcriptional activity.

Active transcription correlates with chromatin decompaction in single cells

To directly correlate transcriptional activity with distance measurements on a single-cell level, we applied single-molecule fluorescence in situ hybridization (smFISH) to visualize transcripts as they are produced from the *GAL* locus in our distance reporter strains. We simultaneously used FISH probes for all three *GAL* genes *GAL1*,

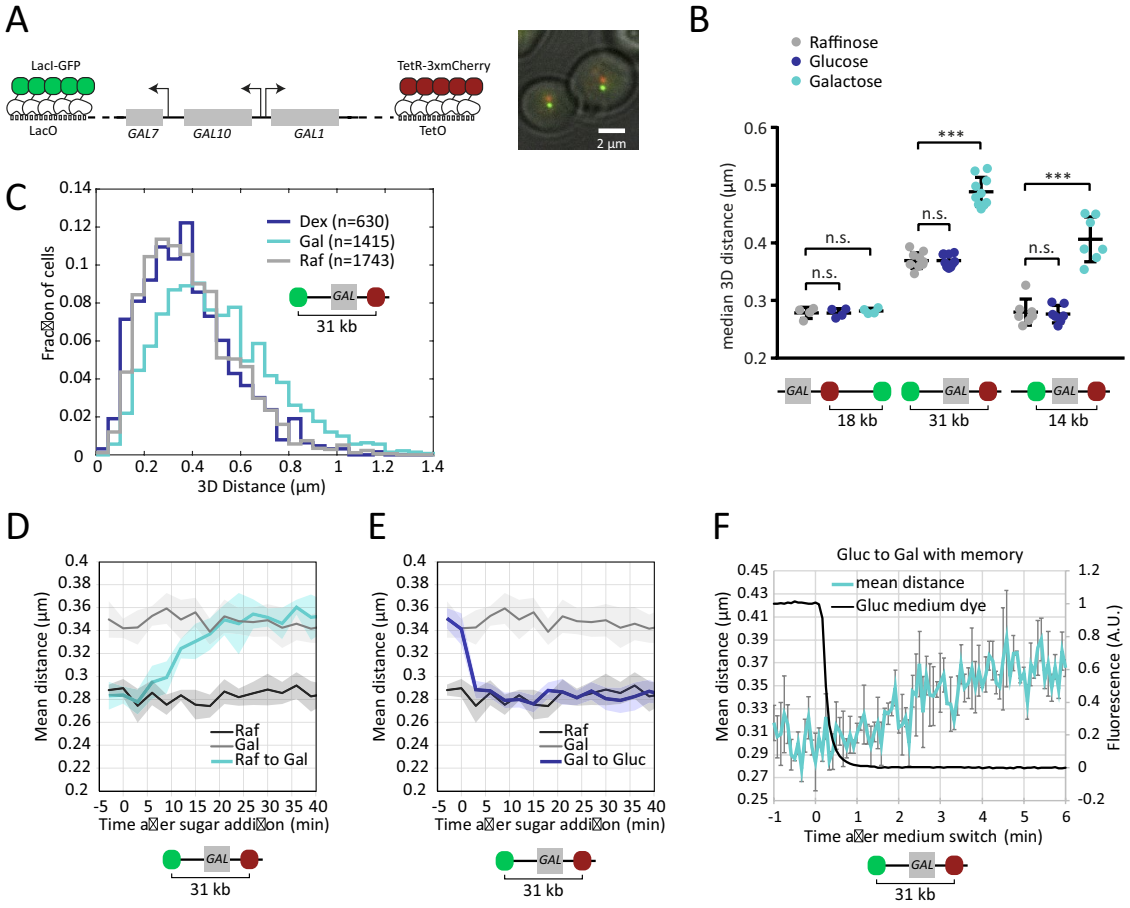

FIGURE 1: Measuring transcription-dependent chromatin decompaction in vivo. (A) Chromosome-labeling scheme with LacO and TetO repeats on either side of the *GAL7-10-1* locus and example image of cells expressing the reporter constructs. (B) The distance between LacO and TetO repeats in cell populations 1 h after addition of the indicated carbon source to the raffinose-containing culture medium. Each dot represents the median from an independent experiment with at least 100 analyzed cells (typically 600–1000). Lines and error bars indicate means and standard deviations. *** adjusted p value < 0.001, n.s. not significant ($p > 0.05$). (C) Histogram of distance distribution for TetR and LacI dots for 31-kb reporter strain in raffinose (gray), glucose (dark blue), or galactose (light blue). Shown is one biological replicate from B. (D) Mean distance of cell population during addition of galactose to cells grown in raffinose (or continuous growth in either galactose or raffinose). Shown is the mean of four independent experiments; shaded areas indicate the standard error (SE). In each experiment, >100 cells were analyzed per time point. (E) Mean distance of cell population during addition of glucose to cells grown in galactose (or continuous growth in either galactose or raffinose). Shown is the mean of four independent experiments; shaded areas indicate the SE. In each experiment, >100 cells were analyzed per time point. (F) Mean distance of cell population during medium switch from glucose to galactose. Cells were preinduced by overnight growth in galactose and then grown in glucose for 1 h. Black curve shows fluorescence of Dextran-Alexa Fluor 680 (3000 MW, anionic) present in the glucose medium to monitor the medium switch in the microfluidics setup. Shown is the mean of three independent experiments; error bars indicate the SE. Note high fluctuation due to low cell numbers (30–50 per time point and experiment).

GAL10, and *GAL7*, all labeled with the same fluorophore (Qasar670). While cytoplasmic mRNAs are visible as individual spots or as hazy signals due to the large numbers of molecules in induced cells, the transcription site is visible as a bright focus in the nucleus close to the repeat-marked gene loci (Figure 2A). Transcription spots and cytoplasmic mRNA foci are absent in cells grown in raffinose (Figure 2A, first panel). Upon induction with galactose, the fraction of cells with transcription spots increased over the course of 30 min, mirroring the increase in the mean distance in the population after induction (Figure 2B). After 60 min or longer, a transcription spot can be seen in virtually every cell (Figure 2A), but since our automatic detection routine does not detect all transcription spots, the maximum measured percentage of cells with transcription spots was only ~80% (Figure 2B).

To correlate transcription with distance, we analyzed early time points after induction, when only a fraction of the cells showed a transcription spot (Figure 2B). We separately determined the 3D distance between the LacO- and TetO-repeat markers in cells with or without a detectable transcription spot. At 5 min after induction, decompaction was still minimal and we observed only few cells with a transcription spot. However, after 10 and 30 min, the distances in cells with transcription spots were significantly larger than in cells without transcription spots (Figure 2, C and D). Thus, decompaction correlates with transcription also on a single-cell level.

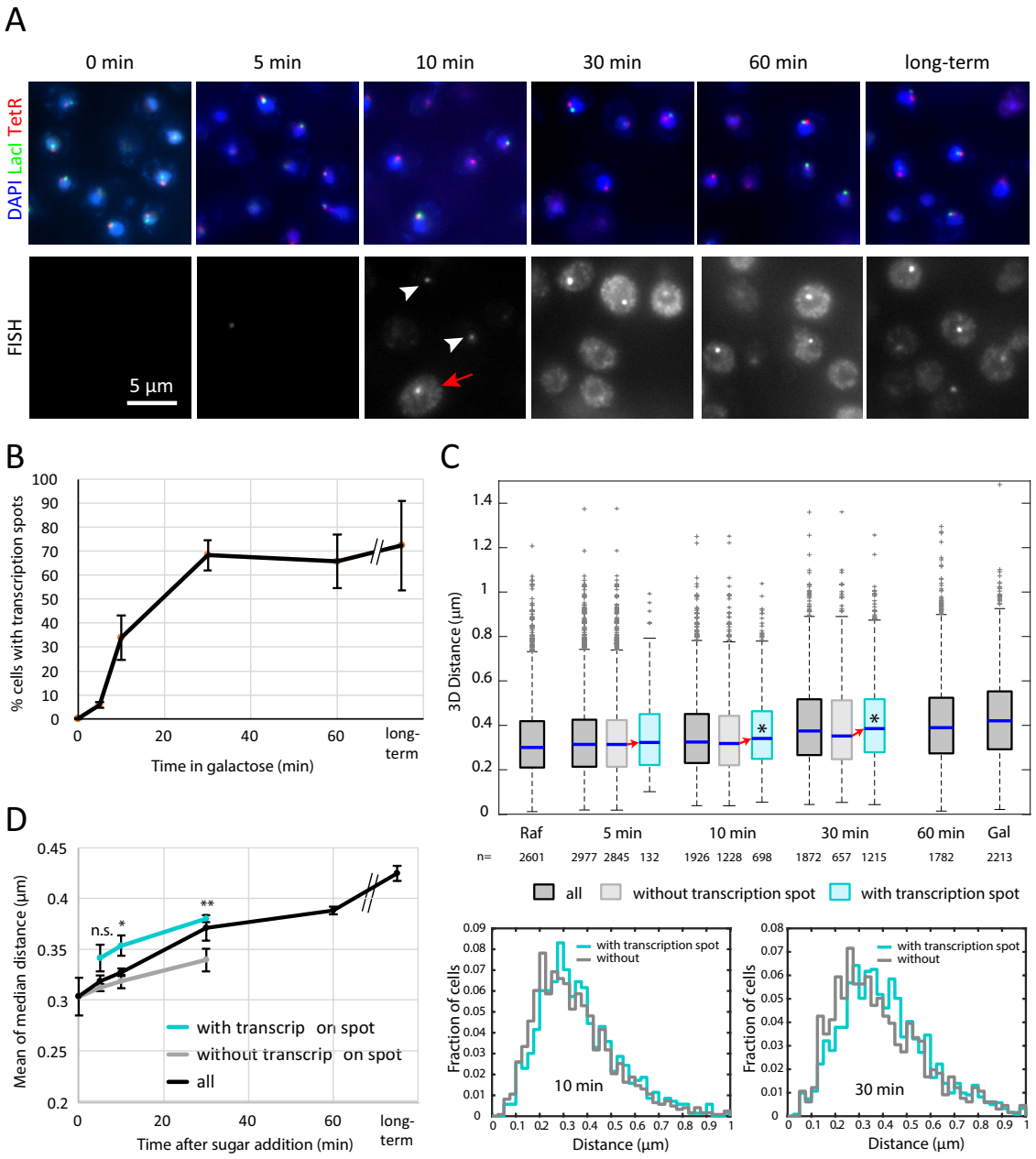

FIGURE 2: Chromatin opening correlates with transcription on single-cell level. (A) Individual slices of image stacks showing smFISH signal (bottom) in cells expressing genomic markers (green and red) and stained with DAPI (4′,6-diamidine-2′-phenylindole dihydrochloride, blue) grown in raffinose (0 min) or after different times of induction with galactose. The cells were hybridized with probes against *GAL1*, *GAL7*, and *GAL10* mRNAs simultaneously, all labeled with the far-red dye Qasar670. In the image of the 10-min time point, two transcription spots in cells with little cytoplasmic mRNA signal are indicated by white arrowheads, and a cell with many cytoplasmic mRNA foci is indicated with a red arrow. (B) Quantification of percentage of cells in which a bright transcription spot could be detected (mean of three biological replicates; error bars indicate SD). (C) Distribution of distances across the *GAL* locus for all cells (dark gray) and cells without (light gray) or with (light blue) transcription spot. Stars indicate that the median of the distances in cells classified as carrying a transcription spot is outside the 95% confidence interval of the median of the distances in cells classified as not carrying a transcription spot and vice versa. *n*: number of cells analyzed. Histograms below show comparison of distance distributions at 10 and 30 min after induction. Shown are the data of one representative experiment out of three biological replicates. (D) Means of median distances in cells classified for absence or presence of a transcription spot from three biological replicates (error bars represent SD). Difference between populations with and without spots was tested using an unpaired 2-tailed *t* test not assuming equal variance. n.s. $p > 0.05$, *$p < 0.05$, **$p < 0.01$.

After transcriptional repression by the addition of glucose, the signal of *GAL* mRNAs in the cytoplasm quickly diminished (Supplemental Figure 3A). Although the nuclear FISH signal at the site of transcription was reduced as well, a weak spot could still be detected in many cells even 60 min after glucose addition (Supplemental Figure 3, A and C). Most likely this corresponds to polyadenylated *GAL* mRNAs that were previously reported to persist at the *GAL* gene loci upon transcriptional shutoff (Abruzzi *et al.*, 2006). Interestingly, cells with

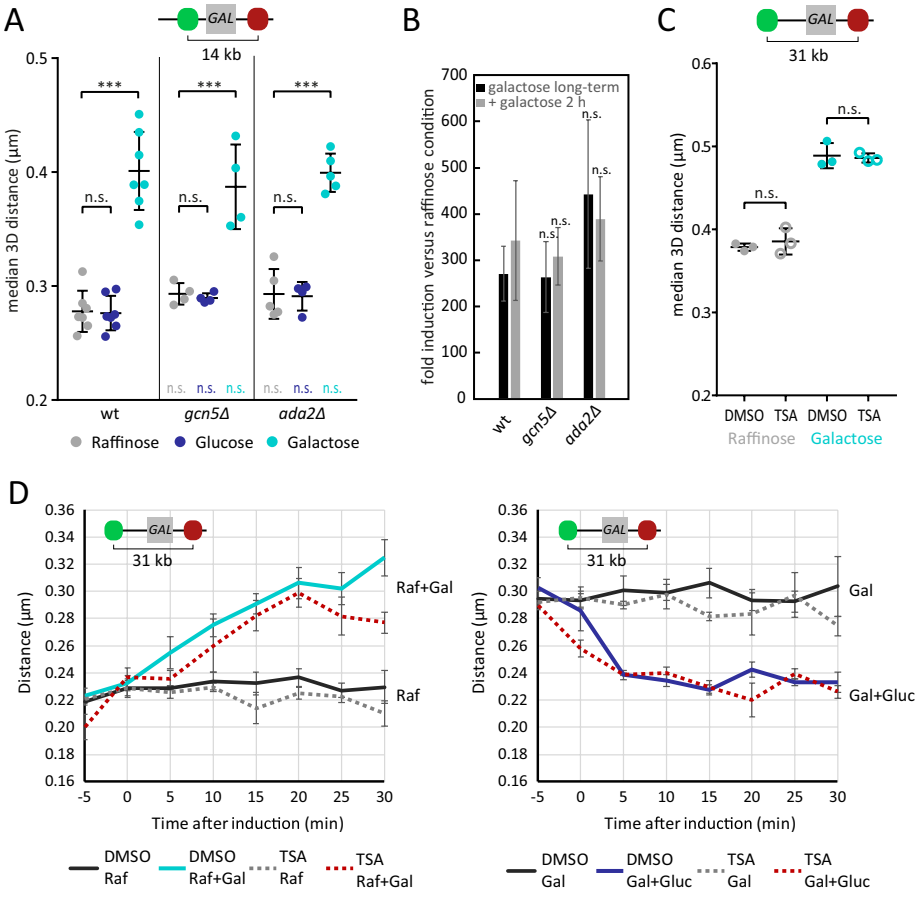

FIGURE 3: The role of acetylation in chromatin opening. (A) The median distance between LacO and TetO repeats in cell populations 1 h after addition of the indicated carbon source to the raffinose-containing culture medium to a final concentration of 2% (raffinose 4%). Each dot represents the median of an independent experiment with at least 200 analyzed cells (typically 600–1000). Lines and error bars indicate means and standard deviations. *** adjusted p value < 0.001, n.s. not significant ($p > 0.05$). Colored n.s. indicates that there is not a significant difference from the wild type (wt) under the same condition. (B) Fold induction of *GAL10* mRNA compared with growth in raffinose determined by qPCR (normalized for *ACT1* mRNA as endogenous control). Means of three to four biological replicates are shown. Error bars represent SE. (C) The median distance between LacO and TetO repeats in cell populations in steady state growth in medium containing 2% galactose or 2% raffinose. Each dot represents the median of an independent experiment with at least 300 analyzed cells (typically 600–1000). Lines and error bars indicate means and standard deviations. n.s. not significant. (D) Opening and closing kinetics in the presence of TSA or DMSO. Cultures grown for 16 h in the presence of DMSO or TSA were diluted 1:1 with medium containing TSA or DMSO, respectively, as well as 4% glucose or galactose to obtain a final concentration of 2% in the medium. Mean of three biological replicates is shown; error bars represent standard error of the mean. More than 100 cells were analyzed per time point in each condition and experiment.

brighter RNA dots showed a distance distribution shifted to longer distances than in cells with a weaker or absent RNA dot signal (Supplemental Figure 3B). This might indicate that transcription is still ongoing in those cells and thus the brighter RNA signal could stem from nascent transcripts. Alternatively, long-lived, chromatin-associated RNAs might contribute to keeping chromatin in a partially decompacted state.

Histone acetylation is dispensable for chromatin decompaction at the *GAL* locus

The increased distance distribution observed in our assay, which is indicative of decompaction of chromatin during transcription, could originate from reduced internucleosomal interactions, from the eviction of nucleosomes, or from both. Internucleosomal interactions are often mediated by histone tails and are thought to be regulated by posttranslational modification. Histones H3 and H4 contribute most to direct internucleosomal interactions but are also required for the recruitment of transcriptional activators. Acetylation of H3 in vivo occurs predominantly through Gcn5 (Grant *et al.*, 1997). This histone acetyl transferase is a component of the SAGA complex, which is recruited to the *GAL* locus by the transcriptional activator Gal4 (Carrozza *et al.*, 2002; Govind *et al.*, 2007). However, neither the deletion of the SAGA histone acetyl transferase Gcn5 nor that of its activating subunit Ada2 influenced chromatin decompaction across the *GAL* locus (Figure 3A). These mutations also do not affect preinitiation-complex formation at the *GAL* promoter (Bhaumik and Green, 2001) or mRNA production (Stafford and Morse, 2001; Green *et al.*, 2012; Figure 3B), suggesting that acetylation is dispensable for transcriptional activation and chromatin decompaction induced by Gal4. (Note that mRNA expression data normalized to the same conditions in the wild-type strain rather than to the raffinose condition in the same strain are shown in Supplemental Figure 4.) While dispensable for activation, Gcn5 activity is crucial for the association of the *GAL* locus with the nuclear periphery upon activation (Dultz *et al.*, 2016). Therefore, our results rule out the possibility that the observed decompaction response is a consequence of relocalization of the *GAL* locus to the nuclear pore complex, which might, for example, generate pulling forces that could lead to stretching of the chromatin fiber.

We also tested whether the inhibition of histone deacetylases using trichostatin A (TSA) would affect chromatin decompaction. TSA treatment neither changed the steady state distance distributions (Figure 3C) nor affected induction or repression kinetics (Figure 3D). Since both the deletion of *GCN5* and the inhibition of histone deacetylases targeted by TSA globally affect acetylation levels of histones (Vogelauer *et al.*, 2000; Supplemental Figure 5A), these results indicate that the global acetylation state of histones per se does not play a major role in regulating chromatin compaction at the *GAL* locus as detected by our assay.

In contrast to the *GAL* genes, other budding yeast genes were previously shown to depend fully on the HAT activity of Gcn5 for their transcriptional activation, including a β-estradiol responsive transcriptional activator based on the viral VP16 transactivation domain (Stafford and Morse, 2001). Intriguingly, we found that upon activation via a β-estradiol–inducible VP16 fusion protein (Louvion *et al.*, 1993), Gcn5 was essential for decompaction (Supplemental

Figure 5, B–D), and neither *gcn5*Δ nor *spt20*Δ cells displayed decompaction of the *GAL* locus upon addition of β-estradiol (Supplemental Figure 5, E and F), suggesting that transcriptional activation and decompaction are closely linked. These data also show that the observed decompaction response is not specific for Gal4-mediated activation.

Mutants that affect transcription also affect decompaction

Although Gcn5 was dispensable for chromatin decompaction, deletion of the SAGA component Spt20, which is required for the stability of the SAGA complex (Grant *et al*., 1997) and for its recruitment by Gal4 (Bhaumik and Green, 2001; Larschan and Winston, 2001; Bryant and Ptashne, 2003), led to strongly reduced decompaction of the *GAL* locus (Figure 4, A and C). As previously reported (Bhaumik and Green, 2001), Spt20 mutants also show strongly reduced *GAL* gene transcription (Figure 4B).

Whereas SAGA is thought to be required to stabilize the general transcriptional coactivator Mediator at the *GAL* promoter, Gal4 is also able to recruit this complex directly (Traven *et al*., 2006). Indeed, cells with a deletion of *GAL11,* a Mediator component that mediates direct interaction with Gal4, or expressing a temperature-sensitive mutant of the Mediator protein Med7 (*med7-163*) phenocopied *spt20*Δ cells by exhibiting reduced overall decompaction in galactose as well as slowed decompaction kinetics (Figure 4, A and C; Supplemental Figure 6).

To analyze the effect of *SPT20* or *GAL11* deletions on a single-cell level, we carried out smFISH. After overnight growth in galactose, most cells displayed cytoplasmic mRNA signals, but the signal was strongly reduced compared with that for wild-type cells (Figure 4D). In addition, the intensity of transcription spots, which were still present in most cells, were reduced on average to ~30% of the wild–type intensity (Figure 4, D and E). Thus, in the mutant cells also, reduced transcription correlates with reduced decompaction of the *GAL* locus. Our results reveal a close linkage between transcriptional activation and decompaction, but they are not sufficient to establish a causality or temporal order between the two processes.

We also attempted to directly address the role of Pol II in decompaction using cells expressing a temperature-sensitive mutant allele of the largest subunit of RNA Pol II, *rpb1-1*. *rpb1-1* cells were induced with galactose 1 h after a shift to the restrictive temperature. Both expression of *GAL10* mRNA and decompaction were reduced but not abolished (Supplemental Figure 7, A and B). Thus, it appears that transcriptional induction at the *GAL* locus is so strong that the temperature-sensitive *rpb1-1* mutant is not fully effective in suppressing decompaction and transcription.

Nucleosome remodelers are required for decompaction

Next, we examined the function of nucleosome remodelers in our decompaction assay. As demonstrated by chromatin immunoprecipitation experiments, histone occupancy in the promoter of transcribed genes—but also in the open reading frame (ORF) of highly transcribed Pol II genes, including the *GAL* genes—is reduced severalfold upon activation (Lee *et al*., 2004; Schwabish and Struhl, 2004; Xin *et al*., 2009). Nucleosome eviction is mediated by the SWI/SNF chromatin remodeling complex and the histone chaperones Asf1 (Antisilencing function 1) and FACT (FAcilitates Chromatin Transcription), a heterodimeric complex consisting of Pob3 and Spt16 (Schwabish and Struhl, 2006, 2007; Venkatesh and Workman, 2015). If the observed decompaction across the *GAL* locus is due to nucleosome eviction, depletion of either of these factors should lead to a reduction of decompaction.

SWI/SNF is a chromatin-remodeling complex with nucleosome sliding and nucleosome eviction activities. At the *GAL* locus, it is required for rapid Pol II recruitment and activation (Kundu and Peterson, 2010). We found that deletion of *SNF2*, encoding the ATPase subunit of the complex, slowed down the kinetics of decompaction and strongly reduced the degree of final decompaction as well (Figure 4, A and C) consistent with a reduction in nucleosome eviction across the locus (Schwabish and Struhl, 2006). Although inactivation of SWI/SNF has previously been reported not to alter steady-state *GAL* gene expression (Lemieux and Gaudreau, 2004), we observed reduced mRNA levels both by qPCR and by smFISH in *snf2*Δ cells (Figure 4, B and D). Again, transcriptional activation and decompaction correlated in this mutant, and we observed both reduced transcription and reduced decompaction. In contrast to the SWI/SNF complex, the chromatin-remodeling complexes INO80 (represented by arp6Δ) and SWR1 (represented by swr1Δ) were required neither for chromatin decompaction nor for transcriptional activation at the *GAL* locus (Figure 4, A and B).

Next, we tested the involvement of the histone chaperones Asf1 and FACT, which have both been implicated in the regulation of the *GAL* genes (Schwabish and Struhl, 2006; Xin *et al*., 2009). Deletion of *ASF1* did not prevent chromatin decompaction in our assay (Figure 5A), which is consistent with previous findings that showed only a small decrease in histone H3 (but not H2B) removal at *GAL* promoters and ORFs (Schwabish and Struhl, 2006). Deletion of ASF1 also did not affect transcriptional activation of *GAL10* (Figure 5B). In contrast, cells carrying temperature-sensitive alleles for either component of the FACT complex (pob3-7 or spt16ts) showed defects in decompaction 1 h after a shift to activating conditions at the restrictive temperature (Figure 5D). While pob3-7 cells exhibited slightly increased distances over the GAL locus already in raffinose and only a moderate additional increase upon activation with galactose, *spt16*ts cells showed no decompaction at the restrictive temperature. Importantly, both strains showed levels of GAL10 mRNA induction similar to those in wild-type cells at both permissive and restrictive temperatures (Figure 5C; note that both mutant and wild-type cells exhibited reduced *GAL10* mRNA induction at 37°C compared with 25°C). Therefore, in the *spt16*ts strain, decompaction and transcription are uncoupled, showing that transcription can occur in the absence of detectable decompaction. Although transcription at 37°C might not proceed as efficiently as at 25°C, there is no added defect in FACT mutants, which are clearly defective in decompaction. Together, these findings indicate that the activities of SWI/SNF and FACT are major sources of decompaction and suggest that nucleosome eviction leads to the increase in distance that we observe across the activated locus. However, we cannot exclude the possibility that processes other than nucleosome eviction and associated with actively transcribing Pol II, including histone tail modifications, contribute to the observed decompaction as well. Importantly, the *spt16*ts mutant shows that the observed decompaction is not required for at least moderate levels of transcription.

Decompaction of the *GAL* locus is transcription-dependent

If the observed decompaction is indeed due to the removal of nucleosomes at the promoter and the ORF, the degree of decompaction is expected to scale with the length of the transcription unit. To test this prediction, we introduced *GAL* promoter–driven reporter genes at a different genomic site ~10 kb telomeric of the native *GAL* locus and measured changes in chromatin distance in the presence or absence of galactose (Figure 6). The *GAL* promoter immediately followed by a terminator sequence did not exhibit a significant decompaction response. In contrast, robust decompaction was

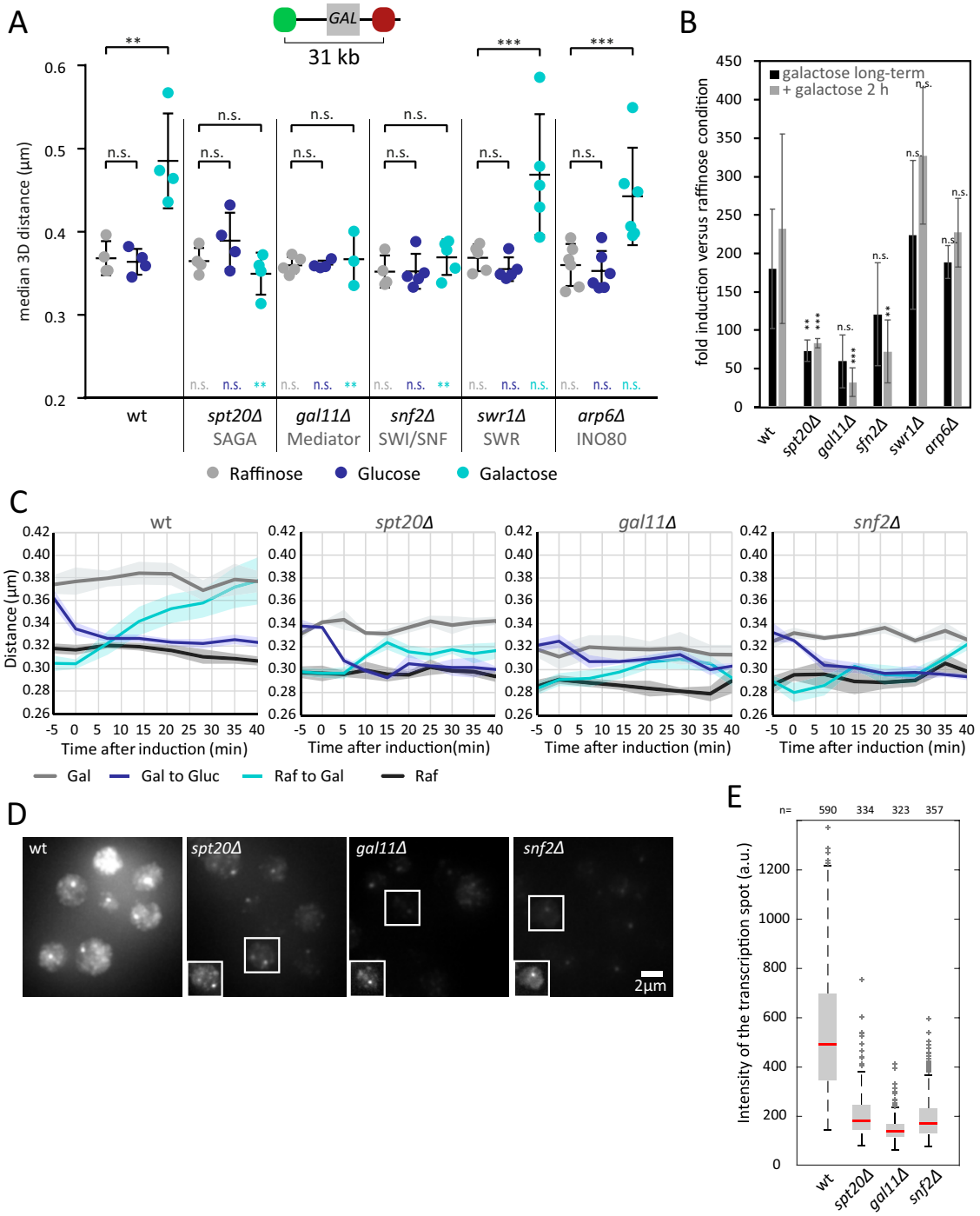

FIGURE 4: Decompaction correlates with transcriptional activation. (A) Distance between LacO and TetO repeats in cell populations 1 h after addition of the indicated carbon source to the raffinose-containing culture medium to a final concentration of 2% (raffinose 4%). Each dot represents the median of an independent experiment with at least 100 analyzed cells (typically 600–1000). Lines and error bars indicate means and standard deviations. *** adjusted p value < 0.001, ** < 0.01, n.s. not significant ($p > 0.05$). Colored p values indicate significance relative to the wild type (wt) under the same condition. (B) Fold induction of *GAL10* mRNA compared with growth in raffinose determined by qPCR (normalized for *ACT1* mRNA as endogenous control). Means of three biological replicates are shown. Error bars represent SE. (C) Kinetics of chromatin opening and closing in wild-type and mutant cells. Cells were grown overnight in medium with 2% raffinose or 2% galactose. Galactose or glucose respectively was added or not added to 2% final concentration at time point 0. Shown are the means of three or more biological replicates with the standard error represented by the shaded areas. (D) smFISH for *GAL1*, *GAL7*, and *GAL10* in the indicated strains growing at steady state in galactose. Insets show enhanced contrast for indicated cells. Images are maximum-intensity projections of z stacks encompassing the entire cells. (E) Box plot showing the intensities of transcriptions spots in the different strains (distribution from one representative experiment out of two biological replicates).

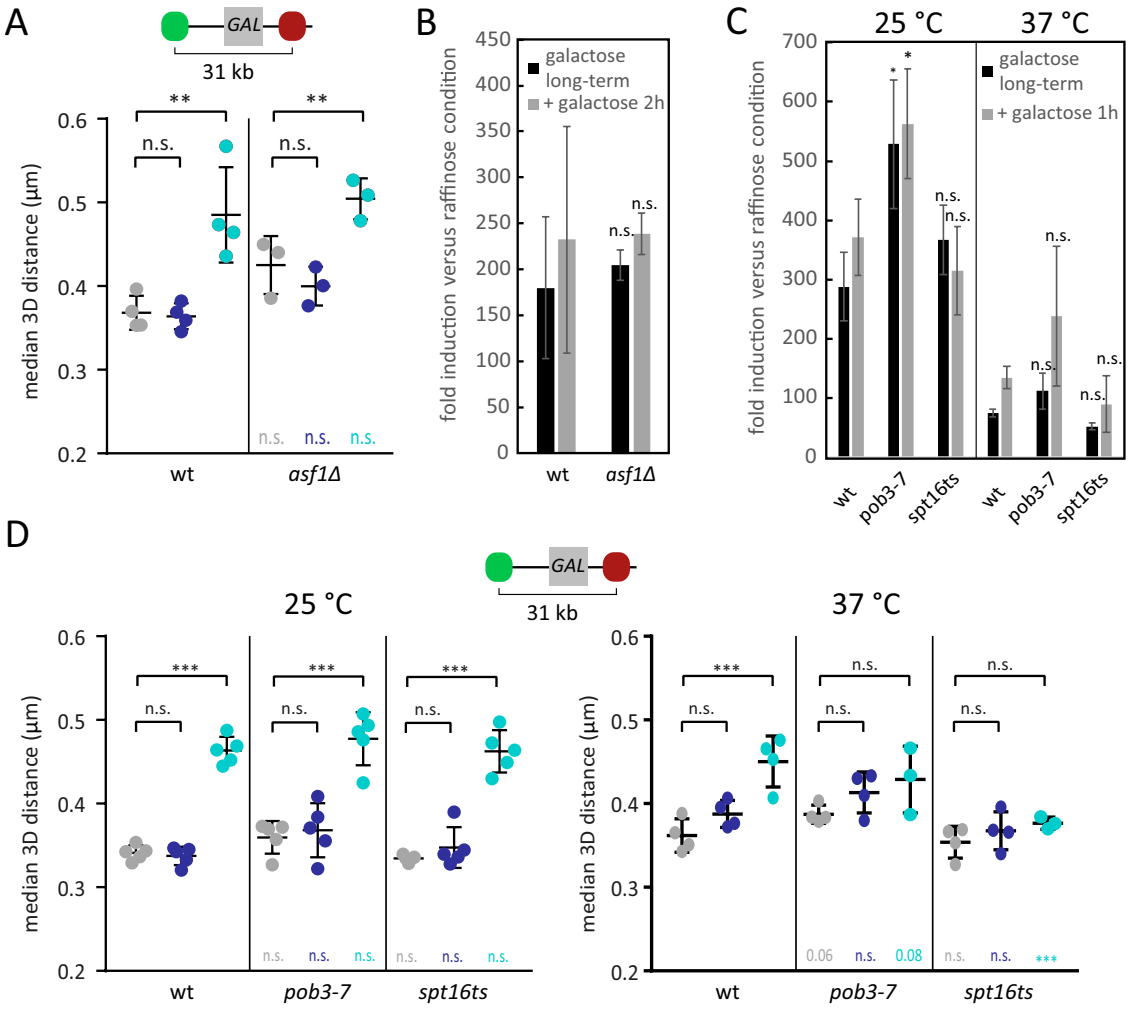

FIGURE 5: Nucleosome chaperones are crucial for chromatin opening. (A) Distance between LacO and TetO repeats in cell populations 1 h after addition of the indicated carbon source to the raffinose containing culture medium to a final concentration of 2% (raffinose 4%). Each dot represents the median of an independent experiment with at least 100 analyzed cells (typically 600–1000). Lines and error bars indicate means and standard deviations. ** adjusted *p* value < 0.01, n.s. not significant ($p > 0.05$). Colored *p* values indicate significance relative to the wild type (wt) under the same condition. (B) Fold induction of *GAL10* mRNA in wild-type and *asf1*Δ cells relative to raffinose growth conditions determined by qPCR (normalized for *ACT1* mRNA as endogenous control). Means of three to four biological replicates are shown. Error bars represent standard errors. (C) Fold induction of *GAL10* mRNA in wild-type cells and cells carrying temperature-sensitive alleles of FACT components relative to raffinose growth conditions determined by qPCR (normalized for *ACT1* mRNA as endogenous control). Means of three to four biological replicates are shown. Error bars represent standard errors. (D) Distance between LacO and TetO repeats in cell populations 1 h after addition of the indicated carbon source to the raffinose-containing culture medium to a final concentration of 2% (raffinose 4%). Cells were cultured in raffinose medium at 25°C and shifted to 37°C for the indicated experiments 1 h prior to addition of the different carbon sources. Each dot represents the median of an independent experiment with at least 200 analyzed cells (typically 600–1000). Lines and error bars indicate means and standard deviations. *** adjusted *p* value < 0.001, n.s. not significant ($p > 0.05$). Colored *p* values indicate significance relative to the wild type (wt) under the same condition.

observed in a strain where the entire *GAL1* gene including promoter and downstream sequences was inserted. Decompaction, although to a weaker extent than for the entire *GAL1* gene, was also observed in a strain where we introduced a *GAL1* promoter–driven ORF coding for glutathione S transferase (GST). Because the ORF of a single *GST* is shorter than that of *GAL1* (700 base pairs vs. 1 kb), we also examined the response in a reporter strain carrying two consecutive copies of the *GST* ORF (*2xGST*). The presence of a second *GST* ORF increased the decompaction to an extent similar to that for the *GAL1* ORF, suggesting that decompaction does indeed scale with ORF length, although a contribution of internal or 3'UTR sequences cannot be excluded.

Decompaction leads to an atypical open chromatin state at the *GAL* locus

Our data provide the first quantitative measurement of transcription-dependent decompaction in living cells. To understand the changes in chromatin structure underlying the observed decompaction response, we analyzed the distance distributions of the populations more closely. The 3D distance of genomic loci on the same

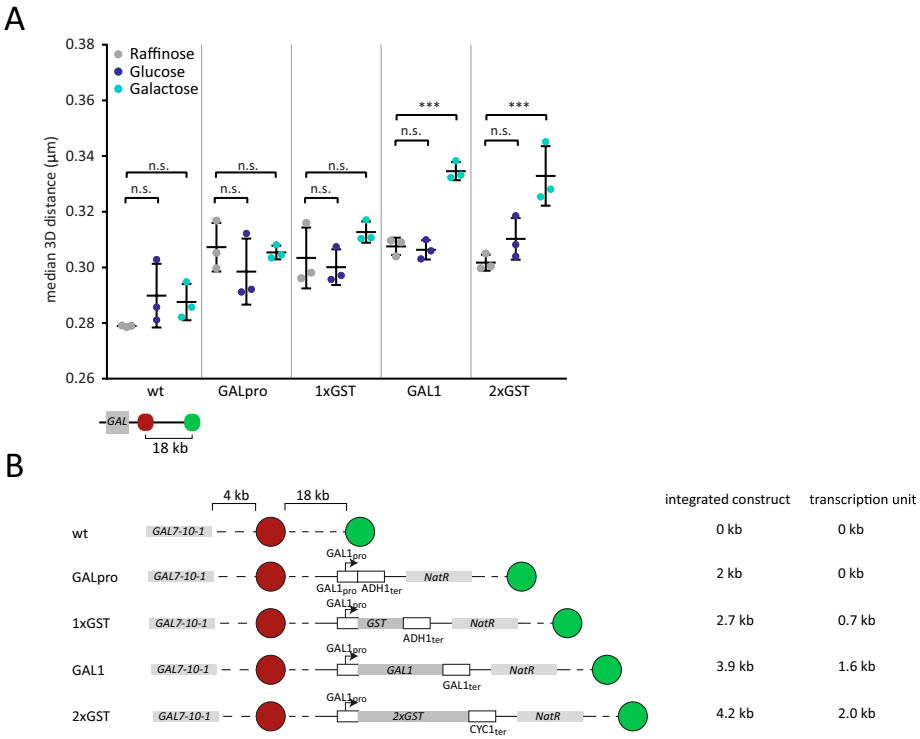

FIGURE 6: Dependence of 3D distance on ORF length. (A) The median distance between LacO and TetO repeats in cell populations 1 h after addition of the indicated carbon source to the raffinose-containing culture medium. Each dot represents the median from an independent experiment with at least 100 analyzed cells (typically 600–1000). Lines and error bars indicate means and standard deviations. *** adjusted p value < 0.001, n.s. not significant ($p > 0.05$). (B) Schematic representation of constructs integrated. Wild-type strain (wt) corresponds to control strain shown in Figure 1B.

chromosome has been shown to scale with the distance in base pairs (van den Engh *et al.*, 1992; Arbona *et al.*, 2017). This is also true on chromosome II of budding yeast in both glucose- and galactose-grown cells, as shown previously by us (Dultz *et al.*, 2016; Figure 7A, gray and black data points). One explanation for the observed changes in compaction at the *GAL* locus could be that the *GAL* locus—compared with bulk chromatin—is *hyper*compacted in the repressed state. However, this is not the case: in the repressed or derepressed state (glucose or raffinose growth), the median distances of TetO and LacO marker pairs across the *GAL* locus (Figure 7A open red circles, data for raffinose grown cells unpublished) are in line with the distances of other pairs of loci on chromosome II. This indicates that the compaction state of the locus is comparable to that of other regions on the same chromosome. In contrast, in galactose-grown cells, the median distance increased far above the distance expected from the linear distance on the chromosome (Figure 7A, filled red circles), showing that the *GAL* locus is strongly *hypo*compacted in its active state. This is consistent with the interpretation that linear decompaction at the *GAL* locus upon transcriptional activation is due to the eviction of nucleosomes and that the high transcriptional activity over three clustered genes at the *GAL* locus leads to a very low histone density and thus hypocompaction.

Because our data provide quantitative measurements of this hypocompaction, we applied computational modeling to predict the level of histone loss that could lead to such a distance increase. To this end, we adapted a previously developed polymer model of the yeast genome, which accurately recapitulates several experimentally determined features (Tjong *et al.*, 2012; Dultz *et al.*, 2016), by increasing the resolution of the model in the proximity of the *GAL* locus. In this model, the compaction of the chromatin fiber in the *GAL* locus had to be reduced by ~60% to recapitulate the observed increase in distances (Figure 7, B and C), which corresponds to a 1.7-fold increase in linear extension. Because the wrapping of DNA on nucleosomes leads to an ~6-fold compaction, this suggests that ~30% of the nucleosomes at the *GAL* locus are evicted upon transcriptional activation. This is in accordance with nucleosome occupancy measurements (Schwabish and Struhl, 2006) and, at a density of 162 base pairs/nucleosome (Horz and Zachau, 1980), corresponds to the eviction of ~11 of 36 nucleosomes across the locus.

DISCUSSION

The recent development of chromosome conformation capture techniques has revolutionized the characterization of 3D interaction landscapes of chromatin and has led to many important discoveries and new models of chromatin organization (reviewed in Pombo and Dillon, 2015; Bonev and Cavalli, 2016). However, these techniques require the fixation of cells and are usually applied to cell populations. Furthermore, it is not possible to convert the interactions detected by chromosome conformation capture directly into 3D distances in the cell nucleus. In fact, a direct comparison of chromosome capture analyses with DNA fluorescence in situ hybridization results has revealed that the two techniques do not always result in congruent findings (Williamson *et al.*, 2014). It is therefore crucial to analyze chromatin conformation in situ and also in vivo.

Chromatin decompaction upon transcriptional activation has been visualized in mammalian cells using large repeat arrays (Tumbar *et al.*, 1999; Dietzel *et al.*, 2004; Verschure *et al.*, 2005; Hu *et al.*, 2009). FISH analysis has also been employed to obtain distance measurements at activated loci (Chambeyron and Bickmore, 2004; Chambeyron *et al.*, 2005; Morey *et al.*, 2007). Although they make important contributions to our understanding of changes in chromatin conformation upon transcriptional activation, quantitative interpretation is limited because fixation and DNA FISH protocols introduce modifications to the cell ultrastructure and repeat arrays may themselves influence the local chromatin environment. Therefore, we have used the budding yeast *S. cerevisiae* to generate a system where live-cell analysis is possible in a quantitative manner at an endogenous gene locus. Although we initially use a three-gene system to establish our assay, we also show that this assay is sensitive enough to visualize decompaction of a single activated gene. Furthermore, the use of budding yeast allows us to study the basic level of chromatin decompaction in the absence of confounding changes in chromatin conformation such as enhancer–promoter looping or looping out from a chromosome territory. Thus, our data yield quantitative measurements of chromatin decompaction upon transcriptional

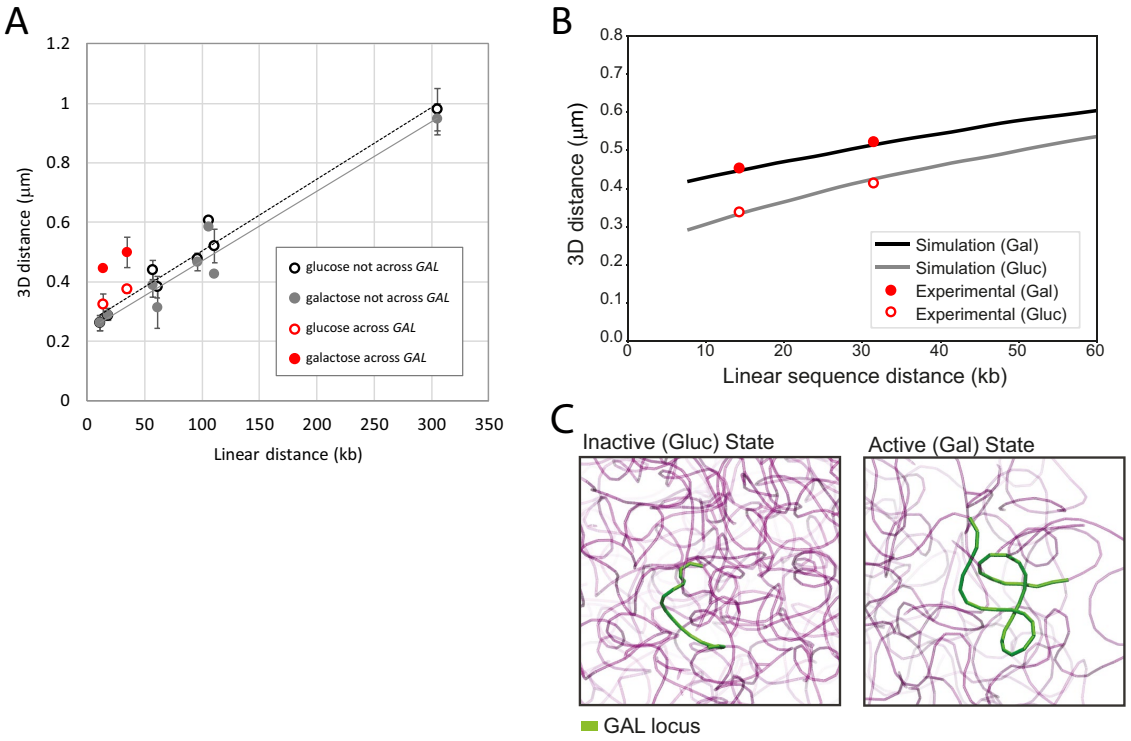

FIGURE 7: Dependence of 3D distance on the linear distance along the chromosome. (A) Experimentally determined mean 3D distance in various strains carrying the chromatin location markers TetO and LacO at different distances from each other on chromosome II. Each data point is the mean of three or more medians from different biological replicates with the SD indicated by the error bars. Gray and black data points are plotted from data published in Dultz *et al.* (2016, Figure 4B). (B) Average 3D distance vs. genomic distance curves obtained from simulated structures at two different values of compaction for the *GAL* locus. The markers correspond to the experimental averages in the active and inactive conditions. To reproduce the experimentally observed 3D distances, the compaction of *GAL* locus was set to 200 and 375 base pairs/bead, respectively, under the active and inactive conditions. (C) Two randomly selected snapshots of the simulated GAL locus under the inactive (Gluc, left panel) and active (Gal, right panel) conditions.

activation and allow us to model the changes in chromatin properties at an activated locus.

The role of acetylation

Interestingly, we found that deletion of the lysine acetyl transferase gene *GCN5* or inhibition of lysine deacetylation by trichostatin A had no observable effect on the distance distribution in our compaction assay. In contrast, the treatment of mammalian cells with TSA was previously reported to affect chromatin organization globally and to lead to decompaction of heterochromatic regions (Toth *et al.*, 2004; Lleres *et al.*, 2009). However, these studies used global histone signals (intensity or FRET-FLIM [Förster resonance energy transfer measured by fluorescence lifetime imaging microscopy]) to assess compaction levels. These analyses thus do not give sequence-specific readout and report on spatial rather than on linear compaction. In agreement with our findings, DNA FISH analysis in mouse cells, which also tested linear compaction between two loci upon TSA treatment, showed decompaction in polycomb silenced regions but not elsewhere (Eskeland *et al.*, 2010). Thus, very low acetylation levels may be crucial for the formation of certain subnuclear compartments in heterochromatic regions of the nucleus but may play a less prominent role in linear decompaction in the relatively open bulk yeast chromatin. Nevertheless, the possibility cannot be excluded that specific acetylation marks added by acetyl transferases other than Gcn5 or removed by non–TSA sensitive deacetylases contributes to linear chromatin decompaction. Furthermore, acetylation could facilitate the binding of factors to specific DNA sequences by rendering the interactions between histones and DNA less tight. This could allow nucleosomes to slide more easily or create binding sites for bromodomain-containing chromatin effector proteins (Filippakopoulos and Knapp, 2014).

The interplay of transcription and decompaction

Our mutant analysis shows that transcriptional activation and chromatin decompaction are tightly coupled. Unfortunately, we could not directly analyze the requirement of transcription per se, since the *rpb1-1* mutant surprisingly did not fully suppress *GAL* gene activation (and decompaction; Supplemental Figure 7). Nevertheless, together with the observation that an ectopic *GAL* promoter in the absence of an ORF was not sufficient to confer decompaction (Figure 6A), our results suggest that ORF transcription by Pol II is required for decompaction of the chromatin at the *GAL* locus. This is consistent with the observation in mammalian cells that only initial decompaction is mediated by transcriptional activation, but that elongation by RNA polymerase is necessary for complete decompaction (Hu *et al.*, 2009). We hypothesize that the removal of nucleosomes at the promoter presents a first stage of decompaction, but elongation and the concomitant eviction of nucleosomes along the ORF constitute the major contribution to chromatin opening. This interpretation is in line with the observation that opening of the *GAL* locus is not detected when both glucose and galactose are present (Figure 4C; galactose+glucose condition), a condition in which SWI/SNF activity has been reported to evict nucleosomes at the promoter (Bryant *et al.*, 2008). However, in addition to the length

of the ORF, the strength of activation and possibly the composition of the 3′ and 5′ UTRs may also contribute to the level of nucleosome eviction and thus decompaction. Importantly, the absence of a decompaction response from the promoter alone also indicates that longer-range interactions mediated by the promoter, such as promoter–enhancer loops, do not play a role in our system, allowing us to focus on the local changes in chromatin organization. Such effects, or the release from higher spatial compaction states, may have contributed to the transcription-independent decompaction that was observed previously in mammalian cells (Hu *et al.*, 2009).

The role of nucleosome eviction

Histones are evicted during transcriptional elongation but repositioned after the passage of Pol II. Both eviction and deposition require the activity of histone chaperones such as FACT. In highly transcribed genes such as the *GAL* genes, individual transcription events follow each other closely (Lenstra *et al.*, 2015). In this case, deposition of histones between rapid rounds of transcription may not be possible, and thus a net loss of histones and nucleosomes occurs. Such a response would explain the dramatic unfolding of chromatin across the *GAL* locus observed in our assay and is consistent with our observation that mutants with reduced transcriptional activity display reduced decompaction. Here, initiation and polymerase II progression occur at lower frequencies, which could allow more time to deposit histones after the passage of Pol II. This interpretation is also in agreement with the observed correlation between ORF length and decompaction.

FACT has previously been shown to be important for nucleosome removal in the *GAL* promoter and ORF. Interestingly, the *spt16*ts mutant allowed us to at least partially uncouple transcription from decompaction: while no detectable decompaction occurred 1 h after induction at the restrictive temperature in this mutant, the mRNA induction was indistinguishable from wild-type cells, indicating that nucleosome and chromatin compaction are not limiting for transcription under these experimental conditions. However, it is possible that higher levels of transcription require nucleosome eviction and decompaction, since even wild-type cells exhibited reduced levels of transcription at the restrictive temperature.

Combined with our modeling results, our data are consistent with the hypothesis that changes in distance are caused by nucleosome eviction. However, we cannot exclude the possibility that additional transcription-associated processes including histone tail modifications or the mRNA transcript itself also provide important contributions to the observed decompaction response.

Outlook

Transcription initiation displays large cell-to-cell variability, and the same can also be expected for decompaction. Unfortunately, we were not able to reliably measure decompaction kinetics on the single-cell level, due to the large fluctuations in distances measured over time even for cells in steady state growth conditions (Shechtman *et al.*, 2017), which is also reflected in the wide distribution of distances in the population at any single time point (Figure 1C). Therefore, further developments of reporter systems with reduced biological noise in combination with improved superresolution microscopy approaches will be needed to enable the analysis of decompaction kinetics on the single-cell level. For example, the contribution of DNA sequences that are not involved in the observed response could be minimized by placing fluorescent reporters directly adjacent to the gene of interest. Adaptations of our system thus have the potential to shed further light on the dynamics of chromatin decompaction by making it possible to study this process quantitatively in single cells under physiological conditions. The data from live-cell microscopy experiments are highly complementary to data obtained from chromosome capture techniques and are very valuable to better understand chromatin organization and its dynamics in vivo. Furthermore, using CRISPR/Cas technologies, our assay could be transferred readily to higher eukaryotic systems. Optimized cassettes for the integration of LacO repeats by CRISPR/Cas have recently been created (Tasan *et al.*, 2017) and the targeting of labeled CIRSPR/Cas complexes (Chen *et al.*, 2013; Chen and Huang, 2014; Ma *et al.*, 2016) will in the future provide a powerful and flexible tool to dissect the contribution of individual players to chromatin compaction in various model systems.

MATERIALS AND METHODS

Plasmid construction

Plasmids were constructed using standard molecular biology techniques. Fragments generated by PCR were verified by sequencing. pKW1008 was constructed by ligating annealed oligos UC586/867 into pFA6-GFP(s65t)-kan (Longtine *et al.*, 1998) using *Pac*I/*Asc*I to replace GFP with a FLAG-tag. pKW2695, pKW2704, and pKW3264 were constructed by ligating PCR products of primers CH4505/CH4506, CH4513/CH4514, or CH6/CH106 on genomic DNA into pKW1689 (Green *et al.*, 2012) after cutting vector and inserting with *Xho*I and *Sac*I. pKW3035 was constructed from a PCR product of UC5681/UC5682 on pKW3010 (Backlund *et al.*, 2014) cut with *Dra*III and ligated into pAFS135 (Straight *et al.*, 1996) also cut with *Dra*III. pKW3681 and pKW3682 were constructed by inserting fragments generated by primers CH1211/CH1213 or CH1211/CH1177 on genomic DNA into the pFA6a backbone containing a NatMx resistance cassette (cut with *Pac*I/*Xho*I). pKW3683 was constructed by inserting into the same vector a stitched PCR product of the *GAL1* promoter (CH1211/CH1218) and GST (CH1214/CH1215) with *Pac*I/*Xho*I. pKW4420 was constructed in multiple steps. The final construct contains homology regions for a region on chromosome II, which were amplified from genomic DNA using primers CH1795/CH1796 and CH1797/CH1798. Between the homology sites, the *GAL1* promoter amplified by CH1211/CH2043 drives a construct encoding 2xGST (CH1789/CH1794 and CH1791/CH1794) tagged with V5. It also contains the NatNT2 resistance cassette for selection and can be integrated after cutting *Not*I/*Asc*I. The Gal4DBD-ER-VP16 activation construct was transferred from the construct published in Louvion *et al.* (1993) into a Ylplac204 backbone with an additional NatMx cassette added for selection in TRP+ strains (pKW3504). All plasmids used in this study are listed in Supplemental Table 1. Primers are listed in Supplemental Table 2.

Yeast strain construction

S. cerevisiae strains were constructed in the background of BY4741 and BY4742 (Brachmann *et al.*, 1998) using standard yeast genetic techniques, by transformation either of a linearized plasmid or of a PCR amplification product with homology to the target site (Baudin *et al.*, 1993). The mutants *spt20*Δ, *gal80*Δ, *gcn5*Δ, *asf1*Δ, *snf2*Δ, *gal11*Δ, *pob3-7*, *spt16ts*, *med7-163*, *rpb1-1*, *gal4*Δ, *swr1*Δ, and *arp6*Δ were constructed by mating of the wild-type strains with the corresponding strains from the MATa, MATα deletion collections (Winzeler *et al.*, 1999), or the MATa temperature-sensitive collection (Li *et al.*, 2011), followed by sporulation and tetrad dissection. *ADA2* was deleted by PCR-directed mutagenesis using primers CH395/CH396 on pKW1008 to generate KWY5104. Reporter strains for the experiments shown in Figure 6A were generated by transformation of KWY4067 with the PCR product of CH1272/CH1273 on pKW3681 (=> KWY6245), pKW3682 (=> KWY6247), or pKW3683 (=> KWY6250).

Genotypes were confirmed by PCR. All yeast strains used in this study are listed in Supplemental Table 3.

Yeast culture conditions

Yeast cells were cultured in complete synthetic medium with 2% of either glucose, galactose, or raffinose at 30°C. Temperature-sensitive mutants were grown at 25°C. Some kinetic experiments with mutants showing significant growth defects were also carried out at 25°C. All experiments were carried out with cells in the exponential growth phase. For microscopy experiments, cells were usually inoculated from saturated cultures into fresh medium and grown overnight to OD_{600} = 0.5–0.8 and then imaged. Alternatively, cells were diluted in the morning and grown for an additional two to three cell cycles before the start of the experiment. Trichostatin A (Sigma catalogue number T8552) was used at 50 µM.

Microscopy

Cells were pregrown in raffinose-containing medium and inoculated in 1 ml in 24-well plates overnight so that they reached an OD_{600} of 0.5–0.8 in the morning. Cells were then transferred to concanavalin A–coated 384-well plates (Matrical).

Three-dimensional microscopy of living cells was carried out on a SpinningDisk microscope (Yokogawa Confocal Scanner Unit CSU-W1-T2) built on a Nikon TiE body and controlled with VisiVIEW software using the dual camera acquisition mode and a 100× NA 1.49 CFI Apo TIRF objective. Cameras were an Orca Flash 4.0 V2 used with 2 × 2 binning or an iXon Ultra EMCCDs (Andor); excitation lasers were a DPSS 488-nm (200-mW) and a diode 561-nm (200-mW) laser. Z scanning was performed in streaming mode with a LUDL BioPrecision2 Piezo Stage with 100 ms exposure per frame. Filters were Dichroic quad-band DAPI/GFP/RFP/CY5, splitting filter to camera ports 561LP, and emission filters GFP/ET525/50 and mCherry ET630/75, respectively. Imaging for Figure 6A was performed on the same system in widefield mode with excitation from Spectra X LED lines at 475 and 542 nm.

Time-lapse and FISH imaging experiments were carried out on a temperature-controlled Nikon Ti Eclipse equipped with a Spectra X LED lamp using a Apochromat VC 100× objective NA 1.4 (Nikon) (filters: Spectra emission filters 475/28 & 542/27 and DAPI/FITC/Cy3/Cy5 Quad HC Filterset with 410/504/582/669 HC Quad dichroic and a 440/521/607/700 HC quadband filter [Semrock]) with exposure times of 50–200 ms. For time lapse experiments, induction with different sugars was carried out on stage after the first imaging time point by mixing with an equal volume of sugar-containing medium. Different fields of view were imaged at each time point to prevent phototoxicity and bleaching.

Microfluidics experiments were carried out using a CellASIC ONIX Microfluidic Platform (Merck Millipore). Cells were loaded in CellASIC ONIX plates for haploid yeast cells (Y04C) with 1 psi for 30 s followed by short pulses (0.5 s) of 3 psi. Medium was constantly flowed across the cells at 3 psi during the entire experiment, while the medium channel that was not used was set to 0.3 psi to prevent backflow of the other medium into the medium well. Upon medium switching, the flow rates of the two channels were reversed. The Dextran-AlexaFluor680 (Molecular Probes D34681) was added to the glucose medium at 0.1 mg/ml to monitor flow and medium switching.

Single-molecule fluorescence in situ hybridization

smFISH was carried out according to (Mugler *et al*., 2016) with slight adaptations. The indicated strains were inoculated in synthetic medium containing 2% raffinose and grown overnight to saturation. The next day, cells were diluted in fresh synthetic complete media containing 2% raffinose or 2% galactose and grown overnight at 30°C to the exponential growth phase (OD_{600} = 0.6–0.8). Cells were then induced by addition of glucose or galactose to a final concentration of 2% and fixed after the indicated time points for 15 min at 30°C and for 15 min at 25°C with 4% paraformaldehyde (EM grade 32% paraformaldehyde aqueous solution; Electron Microscopy Sciences 15714), washed with buffer B (1.2 M sorbitol, 100 mM $KHPO_4$ at pH 7.5, 4 °C), and stored at 4 °C overnight. Cells were then spheroplasted for 20 min using 1% 20T zymolyase in 1.2 M sorbitol, 100 mM $KHPO_4$ at pH 7.5, 20 mM vanadyl ribonuclease complex, and 20 µM β-mercaptoethanol, washed with buffer B to stop the spheroplasting reaction, and then washed into 10% formamide (Merck Millipore S4117) in 2× SSC (saline-sodium citrate buffer prepared from 20× SSC; Life Technologies, AM9624).

Mixtures of DNA probes coupled to Quasar670 (Stellaris, LGC Biosearch, Novato, CA; probes were synthesized by BioCat, Heidelberg, Germany) were used for smFISH, targeting the *GAL1*, *GAL7*, and *GAL10* ORFs (Supplemental Table 4). Per sample, 0.5 µl of each probe mix (stock 25 µM) was mixed with 2 µl of salmon-sperm DNA (10 mg ml^{-1}; Life Technologies, 15632-011) and 2 µl yeast transfer RNA (10 mg/ml; Life Technologies, AM7119). The probe mix was denatured in 50 µl per sample of hybridization buffer F (20% formamide, 10 mM $NaHPO_4$ at pH 7.0) for 3 min at 95°C and then mixed with 50 µl per sample hybridization buffer H (4 × SSC, 4 mg/ml BSA [acetylated], and 20 mM vanadyl ribonuclease complex). Cells (approximately corresponding to the pellet of 5 ml initial culture) were resuspended in the hybridization mix and incubated for 8–12 h at 37°C. After four washing steps (10% formamide/2× SSC; 0.1% Triton/2× SSC; 2× SSC/DAPI; 2× SSC), cells were stored at 4°C. Cells were imaged in concanavaline A–coated 384 wells. Microscopy was performed with an inverted epifluorescence microscope (Nikon Ti) equipped with a Spectra X LED light source and a Hamamatsu Flash 4.0 sCMOS camera using a PlanApo 100× NA 1.4 oil-immersion objective and the NIS Elements software. Thirty-one *z* planes were acquired. The stack of the Qasar670 channel was acquired first due to significant bleaching. mCherry and GFP channels were acquired plane by plane to minimize shift between channels.

Image analysis

Images were processed using FIJI (National Institutes of Health ImageJ 1.51p and previous), Diatrack (Vallotton *et al*., 2017), and MATLAB (MathWorks). For 2D analysis of distances on single image planes (for all kinetic experiments shown), positions of chromosome locations marked with LacI or TetR were detected by a 2D Gaussian fit using custom-written scripts in MATLAB (Dultz *et al*., 2016). Distances between detected spots were calculated. Owing to negligible shift between the two channels in these data sets, correction was not required. For 3D analysis of distances (data acquired on a dual-camera spinning-disk microscope), positions of chromosome location marked with LacI or TetR were detected in Diatrack in 3D using across-color tracking to pair corresponding spots from the same cell (parameters used: "exclude blurred," 0.07–0.2, "exclude dim," 20–200, full width half maximum for Gaussian fitting 2.5). Subsequently, positions were corrected for shift between the two channels using bead images (1-µm TetraSpeck fluorescent microspheres; ThermoFisher Scientific) acquired under identical imaging conditions. For shift correction, the field of view was subdivided into 150 × 150–pixel large squares and the mean shift for beads acquired in this region was applied to correct the positions of chromosome locations acquired in this region of the camera. The distances between corrected positions were calculated and used for further analysis. For

FISH analysis, positions of chromosome locations marked with LacI or TetR were detected in Diatrack in 3D using across-color tracking to pair corresponding spots from the same cell. Positions of transcription spots were detected on maximum intensity projections of the Qasar670 channel in Diatrack (parameters: remove dim 200, remove blurred 0.09–0.1, high precision fitting 2.5) and used to categorize cells as having or not having a transcription spot for separate analysis of the two populations. For analysis of transcription spot intensities, transcription spots were detected on 3D stacks in Diatrack and intensity values were obtained from the Diatrack session file. Only the intensity of those transcription spots for which corresponding chromosome locations marked with LacI or TetR could be detected in Diatrack were included in the analysis. Bootstrapping was used to obtain 95% confidence intervals of the medians and mean. Boxplots were plotted in MATLAB using the function boxplot with the default variables: the central line corresponds to the median, the boxes extend from the 25th to the 75th percentile and outliers are defined as data points greater than $q_3 + 1.5 \times (q_3 - q_1)$ or less than $q_1 - 1.5 \times (q_3 - q_1)$. q_1 and q_3 are the 25th and 75th percentiles of the sample data, respectively. The whisker in each case extends to the most extreme data value that is not an outlier. All analysis code is available upon request.

Quantitative real-time PCR

qPCR was performed as described previously (Dultz *et al.*, 2016): cells at OD_{600} 0.8–1 (1 ml) were harvested by centrifugation and snap-frozen in liquid nitrogen. RNA was extracted using the RNeasy kit from Qiagen via mechanical disruption. Total extracted RNA (300 mg) was used for reverse transcription. The RNA was first treated with DNase I using the DNA-free kit from Ambion according to the protocol of the manufacturer. Reverse transcription was performed according to the protocol of the manufacturer using Superscript II reverse transcriptase (Invitrogen) with random hexamer primers. qPCR was performed on a StepOnePlus Instrument (Invitrogen) using Absolute Blue QPCR Mix with SYBR Green and ROX (ThermoFisher Scientific). All experiments were carried out in three technical replicates and three biological replicates. Data were analyzed by the comparative CT method using *ACT1* as endogenous control. Primers used for qPCR are listed in Supplemental Table 2.

Western blotting

For Western blotting, cells were grown in the presence of plain synthetic medium with 2% raffinose or 2% galactose (supplemented as indicated with 1% DMSO [dimethyl sulfoxide] or 1% DMSO + 50 µM TSA) for 16 h to log phase and harvested by centrifugation. Cells were lysed with 0.1 M NaOH and resuspended in reducing sample buffer. The equivalent of 1–2 OD_{600} of culture was separated on a 15% SDS–PAGE, blotted onto a nitrocellulose membrane, and labeled with an antibody against anti-acetylated proteins (Cell Signaling #9441) at 1:1000 dilution and anti-Fibrillarin antibody (ThermoFisher Scientific 38F3) at 1:2000 dilution. Secondary antibodies were goat anti–mouse-Alexa680 (ThermoFisher Scientific A-21057) used at 1:10,000 dilution and goat anti–rabbit-IRDye800 (Rockland) used at 1:5000 dilution. Staining was visualized on an Odyssey CLx Infrared Imaging System (Li-Cor).

Statistical analysis

The effects of treatment and strain on the median distance value in 3D measurements or on fold induction in gene expression measurements were quantified and statistically tested using a linear mixed-effect model with strain and treatment as fixed effects and the experimental day as random effect. The function lmer() of the package lme4 of the program R was used (Bates *et al.*, 2015; Team, 2017). Reported corrected *p* values were computed by post hoc tests using the function glht() of the package multcomp of the program R (Hothorn *et al.*, 2008).

Computational modeling

Average spatial distances were calculated from ensembles containing 1000 structure models of the entire haploid yeast genome. Ensembles were generated for each of the two *GAL* locus activation states (active/galactose and inactive/glucose), as described in Tjong *et al.* (2012) and Dultz *et al.* (2016). All chromosomes were modeled as chains of connecting beads subject to a number of spatial restraints. In particular, all chromosomes were confined inside a nucleus with a radius of 1 µm; the nucleolus and spindle pole body are placed on opposite sides of the nucleus along the central nuclear axis; all nonribosomal-DNA gene regions are excluded from the nucleolar volume; centromeric regions are proximal to the spindle pole body, whereas telomeric regions are tethered to the nuclear envelope (allowing a maximal distance between telomeres and the nuclear envelope of 50 nm). Each bead accommodated ~3.2 kb of genome sequence as described in Tjong *et al.* (2012).

To reproduce the experimental data, we modeled a gradual decrease in chromatin compaction in the proximity of the *GAL* locus. For the 60-kb region starting at the position of the *GAL* locus, the compaction ratio was set to 1.6 kb per bead. We then determined the optimal chromatin compaction for the 6.2-kb *GAL* locus so that the models reproduced most closely the experimentally observed 3D fluorophore distances in both activation states. The *GAL* locus compaction in the inactive glucose state was found to be ~375 base pairs/bead, whereas in the active galactose state it was set to ~200 base pairs/bead.

Each ensemble of genome structures was generated from 1000 independent simulations, each starting from random configurations. The optimization procedure consisted of a simulated annealing molecular dynamics run followed by conjugate gradients score minimization, both performed using IMP (Russel *et al.*, 2012).

ACKNOWLEDGMENTS

We are grateful to R. Sachdev, A. Kralt, S. Heinrich, and other members of the Weis laboratory for critical discussions and suggestions on the manuscript. We thank Joachim Hehl from the Scientific Center for Optical and Electron Microscopy of ETH Zürich (ScopeM) for support with microscopy and Andreas Steingötter from the Statistical Consulting Group at ETH Zürich for help with statistical analysis. This work was supported by the Swiss National Fond (SNF 159731) and the National Institutes of Health (U54DK107981 to F.A.).

REFERENCES

Abruzzi KC, Belostotsky DA, Chekanova JA, Dower K, Rosbash M (2006). 3′-end formation signals modulate the association of genes with the nuclear periphery as well as mRNP dot formation. EMBO J 25, 4253–4262.

Arbona JM, Herbert S, Fabre E, Zimmer C (2017). Inferring the physical properties of yeast chromatin through Bayesian analysis of whole nucleus simulations. Genome Biol 18, 81.

Backlund MP, Joyner R, Weis K, Moerner WE (2014). Correlations of three-dimensional motion of chromosomal loci in yeast revealed by the double-helix point spread function microscope. Mol Biol Cell 25, 3619–3629.

Bates D, Machler M, Bolker BM, Walker SC (2015). Fitting linear mixed-effects models using lme4. J Stat Softw 67, 1–48.

Baudin A, Ozier-Kalogeropoulos O, Denouel A, Lacroute F, Cullin C (1993). A simple and efficient method for direct gene deletion in *Saccharomyces cerevisiae*. Nucleic Acids Res 21, 3329–3330.

Bhaumik SR, Green MR (2001). SAGA is an essential in vivo target of the yeast acidic activator Gal4p. Genes Dev 15, 1935–1945.

Bonev B, Cavalli G (2016). Organization and function of the 3D genome. Nat Rev Genet 17, 661–678.
Brachmann CB, Davies A, Cost GJ, Caputo E, Li J, Hieter P, Boeke JD (1998). Designer deletion strains derived from *Saccharomyces cerevisiae* S288C: a useful set of strains and plasmids for PCR-mediated gene disruption and other applications. Yeast 14, 115–132.
Bryant GO, Prabhu V, Floer M, Wang X, Spagna D, Schreiber D, Ptashne M (2008). Activator control of nucleosome occupancy in activation and repression of transcription. PLoS Biol 6, 2928–2939.
Bryant GO, Ptashne M (2003). Independent recruitment in vivo by Gal4 of two complexes required for transcription. Mol Cell 11, 1301–1309.
Carrozza MJ, John S, Sil AK, Hopper JE, Workman JL (2002). Gal80 confers specificity on HAT complex interactions with activators. J Biol Chem 277, 24648–24652.
Chambeyron S, Bickmore WA (2004). Chromatin decondensation and nuclear reorganization of the HoxB locus upon induction of transcription. Genes Dev 18, 1119–1130.
Chambeyron S, Da Silva NR, Lawson KA, Bickmore WA (2005). Nuclear re-organisation of the Hoxb complex during mouse embryonic development. Development 132, 2215–2223.
Chen B, Gilbert LA, Cimini BA, Schnitzbauer J, Zhang W, Li GW, Park J, Blackburn EH, Weissman JS, Qi LS, Huang B (2013). Dynamic imaging of genomic loci in living human cells by an optimized CRISPR/Cas system. Cell 155, 1479–1491.
Chen B, Huang B (2014). Imaging genomic elements in living cells using CRISPR/Cas9. Methods Enzymol 546, 337–354.
Chen C, Lim HH, Shi J, Tamura S, Maeshima K, Surana U, Gan L (2016). Budding yeast chromatin is dispersed in a crowded nucleoplasm in vivo. Mol Biol Cell 27, 3357–3368.
Dietzel S, Zolghadr K, Hepperger C, Belmont AS (2004). Differential large-scale chromatin compaction and intranuclear positioning of transcribed versus non-transcribed transgene arrays containing beta-globin regulatory sequences. J Cell Sci 117, 4603–4614.
Dultz E, Tjong H, Weider E, Herzog M, Young B, Brune C, Müllner D, Loewen C, Alber F, Weis K (2016). Global reorganization of budding yeast chromosome conformation in different physiological conditions. J Cell Biol 212, 321–334.
Eskeland R, Freyer E, Leeb M, Wutz A, Bickmore WA (2010). Histone acetylation and the maintenance of chromatin compaction by Polycomb repressive complexes. Cold Spring Harb Symp Quant Biol 75, 71–78.
Even-Faitelson L, Hassan-Zadeh V, Baghestani Z, Bazett-Jones DP (2016). Coming to terms with chromatin structure. Chromosoma 125, 95–110.
Filippakopoulos P, Knapp S (2014). Targeting bromodomains: epigenetic readers of lysine acetylation. Nat Rev Drug Discov 13, 337–356.
Fussner E, Strauss M, Djuric U, Li R, Ahmed K, Hart M, Ellis J, Bazett-Jones DP (2012). Open and closed domains in the mouse genome are configured as 10-nm chromatin fibres. EMBO Rep 13, 992–996.
Govind CK, Zhang F, Qiu H, Hofmeyer K, Hinnebusch AG (2007). Gcn5 promotes acetylation, eviction, and methylation of nucleosomes in transcribed coding regions. Mol Cell 25, 31–42.
Grant PA, Duggan L, Cote J, Roberts SM, Brownell JE, Candau R, Ohba R, Owen-Hughes T, Allis CD, Winston F, *et al*. (1997). Yeast Gcn5 functions in two multisubunit complexes to acetylate nucleosomal histones: characterization of an Ada complex and the SAGA (Spt/Ada) complex. Genes Dev 11, 1640–1650.
Green EM, Jiang Y, Joyner R, Weis K (2012). A negative feedback loop at the nuclear periphery regulates GAL gene expression. Mol Biol Cell 23, 1367–1375.
Horz W, Zachau HG (1980). Deoxyribonuclease II as a probe for chromatin structure. I. Location of cleavage sites. J Mol Biol 144, 305–327.
Hothorn T, Bretz F, Westfall P (2008). Simultaneous inference in general parametric models. Biom J 50, 346–363.
Hsieh TH, Weiner A, Lajoie B, Dekker J, Friedman N, Rando OJ (2015). Mapping nucleosome resolution chromosome folding in yeast by Micro-C. Cell 162, 108–119.
Hu Y, Kireev I, Plutz M, Ashourian N, Belmont AS (2009). Large-scale chromatin structure of inducible genes: transcription on a condensed, linear template. J Cell Biol 185, 87–100.
Kundu S, Peterson CL (2010). Dominant role for signal transduction in the transcriptional memory of yeast GAL genes. Mol Cell Biol 30, 2330–2340.
Larschan E, Winston F (2001). The *S. cerevisiae* SAGA complex functions in vivo as a coactivator for transcriptional activation by Gal4. Genes Dev 15, 1946–1956.
Lau MS, Schwartz MG, Kundu S, Savol AJ, Wang PI, Marr SK, Grau DJ, Schorderet P, Sadreyev RI, Tabin CJ, Kingston RE (2017). Mutation of a nucleosome compaction region disrupts Polycomb-mediated axial patterning. Science 355, 1081–1084.
Lee CK, Shibata Y, Rao B, Strahl BD, Lieb JD (2004). Evidence for nucleosome depletion at active regulatory regions genome-wide. Nat Genet 36, 900–905.
Lemieux K, Gaudreau L (2004). Targeting of Swi/Snf to the yeast GAL1 UAS G requires the Mediator, TAF IIs, and RNA polymerase II. EMBO J 23, 4040–4050.
Lenstra TL, Coulon A, Chow CC, Larson DR (2015). Single-molecule imaging reveals a switch between spurious and functional ncRNA transcription. Mol Cell 60, 597–610.
Li B, Carey M, Workman JL (2007). The role of chromatin during transcription. Cell 128, 707–719.
Li Z, Vizeacoumar FJ, Bahr S, Li J, Warringer J, Vizeacoumar FS, Min R, Vandersluis B, Bellay J, Devit M, *et al*. (2011). Systematic exploration of essential yeast gene function with temperature-sensitive mutants. Nat Biotechnol 29, 361–367.
Lleres D, James J, Swift S, Norman DG, Lamond AI (2009). Quantitative analysis of chromatin compaction in living cells using FLIM-FRET. J Cell Biol 187, 481–496.
Longtine MS, McKenzie A 3rd, Demarini DJ, Shah NG, Wach A, Brachat A, Philippsen P, Pringle JR (1998). Additional modules for versatile and economical PCR-based gene deletion and modification in *Saccharomyces cerevisiae*. Yeast 14, 953–961.
Louvion JF, Havaux-Copf B, Picard D (1993). Fusion of GAL4-VP16 to a steroid-binding domain provides a tool for gratuitous induction of galactose-responsive genes in yeast. Gene 131, 129–134.
Ma H, Tu LC, Naseri A, Huisman M, Zhang S, Grunwald D, Pederson T (2016). Multiplexed labeling of genomic loci with dCas9 and engineered sgRNAs using CRISPRainbow. Nat Biotechnol 34, 528–530.
Morey C, Da Silva NR, Perry P, Bickmore WA (2007). Nuclear reorganisation and chromatin decondensation are conserved, but distinct, mechanisms linked to Hox gene activation. Development 134, 909–919.
Mugler CF, Hondele M, Heinrich S, Sachdev R, Vallotton P, Koek AY, Chan LY, Weis K (2016). ATPase activity of the DEAD-box protein Dhh1 controls processing body formation. eLife 5, e18746.
New AM, Cerulus B, Govers SK, Perez-Samper G, Zhu B, Boogmans S, Xavier JB, Verstrepen KJ (2014). Different levels of catabolite repression optimize growth in stable and variable environments. PLoS Biol 12, e1001764.
Ou HD, Phan S, Deerinck TJ, Thor A, Ellisman MH, O'Shea CC (2017). ChromEMT: visualizing 3D chromatin structure and compaction in interphase and mitotic cells. Science 357, eaag0025.
Pombo A, Dillon N (2015). Three-dimensional genome architecture: players and mechanisms. Nat Rev Mol Cell Biol 16, 245–257.
Russel D, Lasker K, Webb B, Velazquez-Muriel J, Tjioe E, Schneidman-Duhovny D, Peterson B, Sali A (2012). Putting the pieces together: integrative modeling platform software for structure determination of macromolecular assemblies. PLoS Biol 10, e1001244.
Schwabish MA, Struhl K (2004). Evidence for eviction and rapid deposition of histones upon transcriptional elongation by RNA polymerase II. Mol Cell Biol 24, 10111–10117.
Schwabish MA, Struhl K (2006). Asf1 mediates histone eviction and deposition during elongation by RNA polymerase II. Mol Cell 22, 415–422.
Schwabish MA, Struhl K (2007). The Swi/Snf complex is important for histone eviction during transcriptional activation and RNA polymerase II elongation in vivo. Mol Cell Biol 27, 6987–6995.
Shechtman Y, Gustavsson AK, Petrov PN, Dultz E, Lee MY, Weis K, Moerner WE (2017). Observation of live chromatin dynamics in cells via 3D localization microscopy using Tetrapod point spread functions. Biomed Opt Express 8, 5735–5748.
Shogren-Knaak M, Ishii H, Sun JM, Pazin MJ, Davie JR, Peterson CL (2006). Histone H4-K16 acetylation controls chromatin structure and protein interactions. Science 311, 844–847.
Stafford GA, Morse RH (2001). GCN5 dependence of chromatin remodeling and transcriptional activation by the GAL4 and VP16 activation domains in budding yeast. Mol Cell Biol 21, 4568–4578.
Straight AF, Belmont AS, Robinett CC, Murray AW (1996). GFP tagging of budding yeast chromosomes reveals that protein-protein interactions can mediate sister chromatid cohesion. Curr Biol 6, 1599–1608.
Tasan I, Sustackova G, Zhang L, Kim J, Sivaguru M, HamediRad M, Wang Y, Genova J, Ma J, Belmont AS, Zhao H (2017). CRISPR/Cas9-mediated knock-in of an optimized TetO repeat for live cell imaging of endogenous loci. bioRxiv. https://doi.org/10.1101/162156.

Taylor GC, Eskeland R, Hekimoglu-Balkan B, Pradeepa MM, Bickmore WA (2013). H4K16 acetylation marks active genes and enhancers of embryonic stem cells, but does not alter chromatin compaction. Genome Res 23, 2053–2065.
Team RC (2017). R: a language and environment for statistical computing. In: R Foundation for Statistical Computing, Vienna, Austria.
Tjong H, Gong K, Chen L, Alber F (2012). Physical tethering and volume exclusion determine higher-order genome organization in budding yeast. Genome Res 22, 1295–1305.
Toth KF, Knoch TA, Wachsmuth M, Frank-Stohr M, Stohr M, Bacher CP, Muller G, Rippe K (2004). Trichostatin A-induced histone acetylation causes decondensation of interphase chromatin. J Cell Sci 117, 4277–4287.
Traven A, Jelicic B, Sopta M (2006). Yeast Gal4: a transcriptional paradigm revisited. EMBO Rep 7, 496–499.
Tsompana M, Buck MJ (2014). Chromatin accessibility: a window into the genome. Epigenetics Chromatin 7, 33.
Tumbar T, Sudlow G, Belmont AS (1999). Large-scale chromatin unfolding and remodeling induced by VP16 acidic activation domain. J Cell Biol 145, 1341–1354.
Vallotton P, van Oijen AM, Whitchurch CB, Gelfand V, Yeo L, Tsiavaliaris G, Heinrich S, Dultz E, Weis K, Grunwald D (2017). Diatrack particle tracking software: review of applications and performance evaluation. Traffic 18, 840–852.
van den Engh G, Sachs R, Trask BJ (1992). Estimating genomic distance from DNA sequence location in cell nuclei by a random walk model. Science 257, 1410–1412.
Venkatesh S, Workman JL (2015). Histone exchange, chromatin structure and the regulation of transcription. Nat Rev Mol Cell Biol 16, 178–189.
Verschure PJ, van der Kraan I, de Leeuw W, van der Vlag J, Carpenter AE, Belmont AS, van Driel R (2005). In vivo HP1 targeting causes large-scale chromatin condensation and enhanced histone lysine methylation. Mol Cell Biol 25, 4552–4564.
Vogelauer M, Wu J, Suka N, Grunstein M (2000). Global histone acetylation and deacetylation in yeast. Nature 408, 495–498.
Wang A, Kurdistani SK, Grunstein M (2002). Requirement of Hos2 histone deacetylase for gene activity in yeast. Science 298, 1412–1414.
Williamson I, Berlivet S, Eskeland R, Boyle S, Illingworth RS, Paquette D, Dostie J, Bickmore WA (2014). Spatial genome organization: contrasting views from chromosome conformation capture and fluorescence in situ hybridization. Genes Dev 28, 2778–2791.
Winzeler EA, Shoemaker DD, Astromoff A, Liang H, Anderson K, Andre B, Bangham R, Benito R, Boeke JD, Bussey H, *et al*. (1999). Functional characterization of the *S. cerevisiae* genome by gene deletion and parallel analysis. Science 285, 901–906.
Xin H, Takahata S, Blanksma M, McCullough L, Stillman DJ, Formosa T (2009). yFACT induces global accessibility of nucleosomal DNA without H2A–H2B displacement. Mol Cell 35, 365–376.